IEEE Sensors Council

# A Novel Eddy Current Sensor for Displacement Measurement With High Accuracy and Long Range

Peng Tong, Liang Wu, *Member, IEEE*, Yanchen A, Rui Su, and Yulong Wu

Abstract—To enlarge the measurement range of traditional eddy current displacement sensors, a novel eddy current linear sensor for displacement measurement with high accuracy and long range is proposed in this article. The sensor consists of a stationary component with metal reflection conductors and a movable component with spiral coils. The metal reflection conductors below the movable component will generate an eddy current and radiate an eddy current magnetic field after the high-frequency alternating excitation signal is applied to field spiral coils. The inductive electromotive forces (EMFs) will be generated in inductive spiral coils. The measurement of displacement relies on the inductive EMFs variation of inductive spiral coils caused by the change of coupling areas between the spiral coils and the metal reflection conductors. The absolute positioning is realized by the combination of a coarse measurement channel and a fine measurement channel. The structure and measurement principle are described in detail. A sensor prototype is fabricated by printed circuit board (PCB) technology, and the experiments are carried out. Based on the experimental results, some error sources are analyzed and the sensor is optimized. The experimental results show that the sensor can achieve absolute positioning, and the worst-case error is 6.75 μm within the measurement range of 500 mm.

Index Terms— **Absolute position measurement, eddy current effect, inductive sensor, spiral coils.**
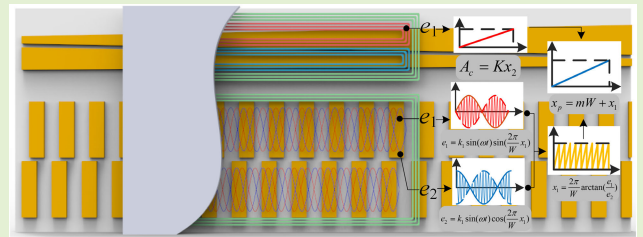
I. INTRODUCTION

MEASUREMENT of wide-range linear displacement with nanometer resolution and micrometer accuracy is vital for various fields, such as precision manufacturing, aerospace industry, and military application [1], [2], [3], [4]. Unlike incremental sensors, absolute sensors can measure the absolute position of a target without calibration and more than 60% of linear displacement sensors currently belong to the absolute types [5], [6], [7], [8]. The main evaluation performance criteria of displacement sensors used are: non-linearity, resolution, sensitivity, compactness, long-term stability, and so on [2], and [9].

The laser interferometer is a typical wide-range measurement system, which uses laser wavelength as the measurement unit [10], [11]. The stabilized interferometers manufactured by Renishaw can realize a linear worst-case error of ± 0.5 ppm with a resolution of 1 nm through an accurate and stable laser source and accurate environmental compensation [12], [13]. However, it is susceptible to beam interference, optical medium variation, and alignment errors, so it is usually used in laboratories to calibrate other sensors or other well-controlled industrial environments [2], [14], [15].

Optical linear encoders can realize high resolution and high accuracy absolute positioning, which adopt the structure of periodic hyperfine grating lines as a measurement standard [16], [17]. Presently, the best commercial absolute optical linear encoder has realized an accuracy of ± 0.5 μm within a 3040 mm range and maintains a high-quality signal by adjusting lighting [18]. Compared with the laser interferometer, optical linear encoders have more robust to the environment and are primarily used in leading-edge manufacturing, accurate measurement equipment, and precision motion control systems [19], [20]. Although many studies have provided some error compensation for the optical linear encoders to improve their worst-case error, they are still limited by ultra-precision engraving technology and the fundamental diffraction limit of the optical scanning method [14], [21].

Capacitive sensors are also applied for absolute positioning, and the displacement is realized by detecting the change of capacitance in the electric field [9], [15]. Capacitive displacement sensors are often used for nanopositioning within the range of hundreds of micrometers [22]. To solve the problem of the limited measurement range of capacitive sensors, some scholars have recently developed capacitive sensors for wide-range absolute measurement [1], [23], [24], [25]. The wide-range capacitive sensor proposed in [26] realizes the worst-case error of ± 200 nm in the measurement range of 200 mm. Capacitive sensors are ubiquitous because of their high precision, good dynamic performance, simple design, and low consumption. However, the permittivity of capacitance is sensitive to environmental variables such as humidity and temperature and exhibits non-linear because of parasitic capacitance and edge effects [5], [27], [28].

Inductive displacement sensors realize displacement measurement by using the change of coil self-inductance or mutual inductance. The inductive displacement sensor reported in [29] consists of two triangular-shaped spiral coils and an E-type soft ferromagnetic core, which realizes 0.4% nonlinearity with 70 mm by detecting the variation of the inductances. The sensors proposed in [30] and [31] consist of bilateral sensing units that realize the original error as low as 15 μm with a range of about 300 mm. In order to improve the time drift stability of inductive sensors, Lu et al. [32] proposed a method combining a magnetic shield ring and resonance circuit. Although inductive displacement sensors have no significant advantages in resolution and accuracy, they are the most preferred sensors in automotive and industrial applications because of their low cost, long life span, and insensitivity to harsh environments [29], [33], [34].

The eddy current displacement sensor based on the eddy current phenomenon is a kind of inductive sensor. The eddy current phenomenon is widely employed in quality detection, fault detection, motion coupling, and other industrial systems [35], [36], [37]. However, the eddy current displacement sensors are widely used in short-range nanopositioning applications owing to their excellent resolution and accuracy. Some of the most advanced custom off-the-shelf eddy current displacement sensors can achieve a resolution of 1.6 nm in the range of 2 mm [9]. Furthermore, the eddy current displacement sensor proposed in [38] has a resolution of 0.6 nm in the measurement range of 10 μm (14.1-bit dynamic range).

To extend the measurement range, a new eddy current linear encoder sensor is proposed in this article, which relies on a repetitive variation of the inductive electromotive force (EMF) against displacement caused by the change of coupling areas between the movable component and the stationary component. Section II introduces the structure and working principles of the sensor in detail. Then, the electromagnetic field simulation of the sensor model is carried out to verify the feasibility of the sensor in Section III. Next, the experimental results are shown and discussed in Section IV. Finally, the conclusions are presented in Section V.
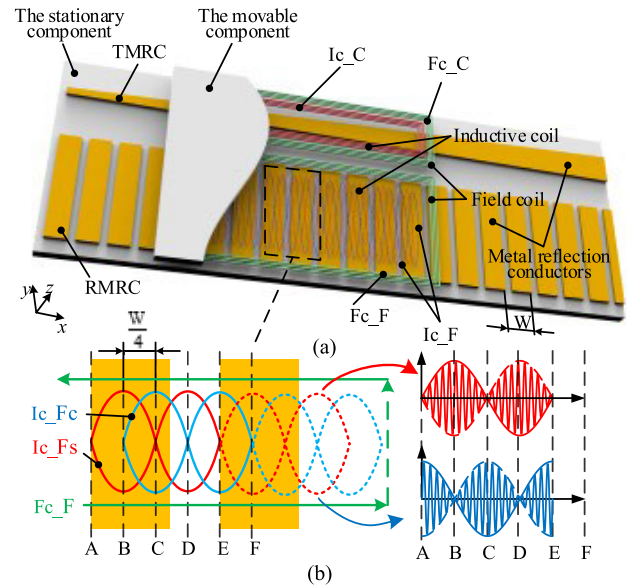

Fig. 1. Structure diagram of the sensor. (a) Overall structure of the sensor. (b) Simplified example of motion coupling and five typical points in the signal-generating process. The position of the five typical points are A(0, 0), B(W/4, 0), C(W/2, 0), D(3W/4, 0), E(W, 0), F(5W/4, 0).

II. STRUCTURE AND MEASUREMENT PRINCIPLE ANALYSIS

A. Structure of the Sensor

A simplified diagram of the proposed absolute eddy current linear encoder sensor is shown in Fig. 1. The sensor consists of a stationary component with metal reflection conductors and a movable component with field coils and inductive coils, and constitutes a coarse measurement channel and a fine measurement channel. The coarse measurement channel is used to realize coarse absolute positioning and the fine measurement channel is used to determine the worst-case error. There are two groups of metal reflection conductors in the stationary component named trapezoidal metal reflection conductors (TMRC) and rectangular metal reflection conductors (RMRCs), which correspond to the coarse measurement channel and fine measurement channel respectively. The RMRCs include N rectangular metal conductors arranged at equal intervals with pitch W.

The spiral coils on the movable component consist of field coils and inductive coils, and the field coils are arranged outside the inductive coils. The field coil and the inductive coil of the coarse measurement channel (Fc_C and Ic_C) both are rectangular spiral coils, arranged directly above the TMRC. The field coil of the fine measurement channel (Fc_F) is also rectangular. The inductive coils of the fine measurement channel consist of a sine inductive coil (Ic_Fs) and a cosine inductive coil (Ic_Fc) and are staggered W/4 along the measurement direction (X-direction).

B. Measurement Principle and Absolute Positioning Method

When the field coils (Fc_C and Fc_F) are supplied with high-frequency alternating signal $I(t)$, a time-varying
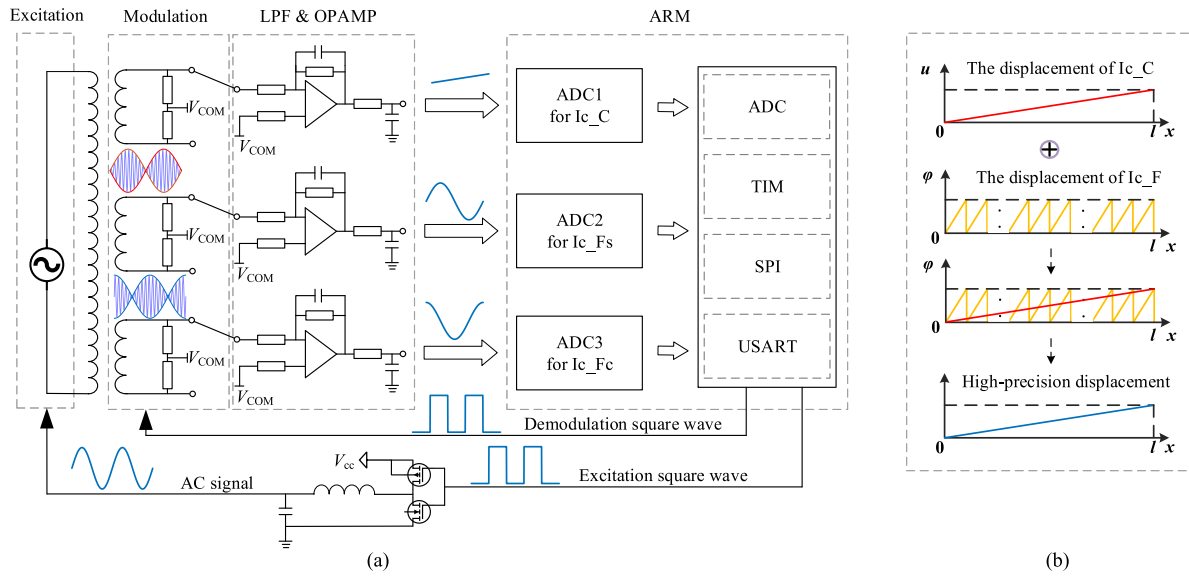
Fig. 2. Signal processing of the sensor. (a) Signal processing. (b) Absolute positioning method.

magnetic field H_1 is generated around the field coils. $I(t) = A_m \sin(\omega t)$, where A_m is the amplitude and ω is the angular frequency. When the metal reflection conductors (RMRC and TMRC) are within the time-varying magnetic field, an eddy current I_2 will be produced on the surface of the metal reflection conductors, then an eddy current magnetic field H_2 will generate to weaken the effects of the time-varying magnetic field H_1. The eddy current I_2 changes periodically when relative displacement occurs between the movable component and the stationary component. The magnetic flux in the inductive coils varies with the eddy current I_2. The change of the magnetic flux is sensed as a change of inductive EMF, so the displacement of the movable component can correspondingly be obtained by processing the inductive EMF variations. As shown in Fig. 1(b), the amplitudes of the EMFs are different when the inductive coils are located at different positions. For clarity, only part of the inductive coils after amplification is shown. The solid line represents the starting position, while the dotted line represents the position of moving a pitch, correspondingly, the regular sine and cosine signals are generated. Five typical positions during the signal-generating process are given in Fig. 1(b). Displacement measurement is realized by the arctangent operation of the two signals.

The absolute position measurement method is illustrated in Fig. 2(b). For the fine measurement channel, the eddy current in the RMRC changes periodically with the displacement, and thus the magnetic flux in the inductive coils also changes periodically. The inductive EMFs of Ic_Fs and Ic_Fc can be shown as follows, whose amplitudes are relational to the displacement:

$$e_{Ic\_Fs}(t, x) = k_1 \sin(\omega t) \sin\left(\frac{2\pi}{W} x_1\right) \tag{1}$$

$$e_{Ic\_Fc}(t, x) = k_1 \sin(\omega t) \cos\left(\frac{2\pi}{W}\left(x_1 + \frac{W}{4}\right)\right)$$

$$= k_1 \sin(\omega t) \cos\left(\frac{2\pi}{W} x_1\right). \tag{2}$$

Here, x_1 is the displacement of the movable component within a pitch of the fine measurement channel. By combining (1) and (2), and adopting the signal processing method of the amplitude discrimination principle, the displacement of x_1 can be shown as follows:

$$x_1 = \frac{W}{2\pi} \arctan\left(\frac{e_{Ic\_Fs}(t, x)}{e_{Ic\_Fc}(t, x)}\right). \tag{3}$$

For the coarse measurement channel, the eddy current induced in the TMRC increases with the increase of the coupling area between the TMRC and the field coils. Correspondingly, the amplitude A_c of the Ic_C also changes linearly, which can be expressed as follows:

$$A_c = K x_2. \tag{4}$$

Here, K is a constant and $K < 0$, x_2 is the displacement. A_F corresponds to the number of pitches, so as to realize the pitch positioning. The number of the fine measurement channel cycles m can be shown as follows:

$$m = \text{floor}\left(\frac{A_c}{x_2 W}\right). \tag{5}$$

Here, floor($\cdot$) returns the greatest integer less than or equal to its argument. Accordingly, the absolute position x_p can be shown as follows:

$$x_p = mW + x_2. \tag{6}$$

C. Signal Processing

The signal processing method based on the amplitude discrimination principle adopted by the sensor is illustrated in Fig. 2(a). Three roads of the square waves with a frequency of 4 MHz are generated by an ARM chip (Model: STM32F373), which are used as excitation signals and demodulation signals. After the excitation square waves are amplified by MOSFET, and a high-quality sinusoidal signal with a frequency of 4 MHz is obtained through LC first-order low-pass filter. The inductive signal is a standing wave signal

TABLE I
PARAMETERS OF SIMULATION SENSOR MODEL

Parameter	Setting
Simulation range	4 mm
Coil turns of field coils	10 turns
DC impedance of field coils	10 Ω
Coil turns of inductive coils	10 turns
DC impedance of inductive coils	1 MΩ
Frequency of AC current	4 MHz
Amplitude of AC current	0.1 A
Linear step	0.2 mm
Time step	10 ns
Material of coils and reflection conductors	Copper
Gap between movable component and stationary component	0.5 mm

Fig. 3. Sensor prototype and experimental platform. (a) Inductive EMF of Ic_Fs. (b) Inductive EMF of Ic_Fc. (c) Inductive EMF of Ic_C. (d) Simulation data after processing.

containing time t and space x. After demodulation, filtering, and amplifying, the inductive EMFs containing displacement information are converted into digital quantity by analog-to-digital modules. The amplitude of the coarse measurement channel increases with the increase of the displacement, so as to realize the pitch positioning. The amplitude of the fine measurement channel increases with the changes periodically with the displacement, and the displacement is obtained by arctangent operation. The sensor communicates with the motor driver via the BissC protocol.

III. SIMULATION OF SENSOR MODEL

According to the structure and measurement principle analysis of the sensor, a 3-D model of the sensor is established and simulated in finite element analysis (FEA) software to verify the feasibility of the sensor. The main simulation parameters are presented in Table I.

Because the FEA results are greatly affected by the model establishment, solution setting, mesh division, and other factors, only qualitative analysis is carried out on the feasibility of the sensor structure and measurement principle, that is, only determine whether the simulation curve is sine or cosine, without considering the magnitude of the curve amplitude. The resistance of inductive coils is set to be 1 MΩ to acquire an output voltage mostly. The air gap between the movable component and the stationary component is 0.5 mm. The stop time is set to be 0.25 μs, and the time step is 0.01 μs. The movable component moves 4 mm in steps of 0.2 mm. The simulation results are shown in Fig. 3. The inductive EMFs of Ic_Fs, Ic_Fc, and Ic_C are standing waves, whose amplitude changes with the displacement and the phase maintains invariability. After processing the simulation data, the variation curve of the inductive voltage amplitude with the displacement is obtained, as shown in Fig. 3(d). The red, blue, and yellow curves represent the EMF of Ic_Fs, Ic_Fc, and Ic_C, respectively, corresponding to (1), (2), and (4) when only x is the independent variable. The simulation results are consistent with the measurement principle, which
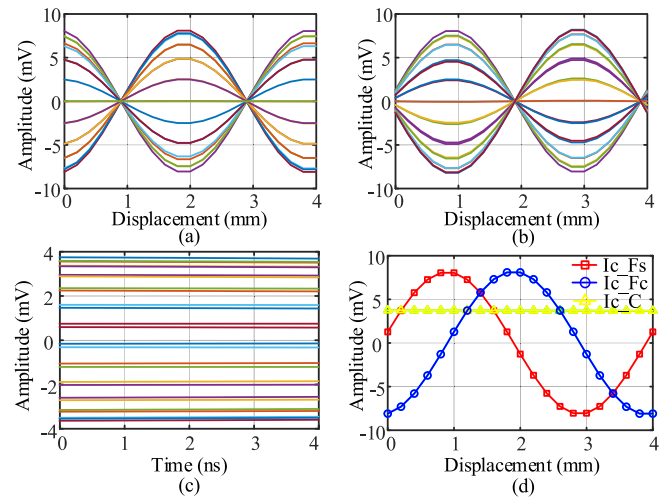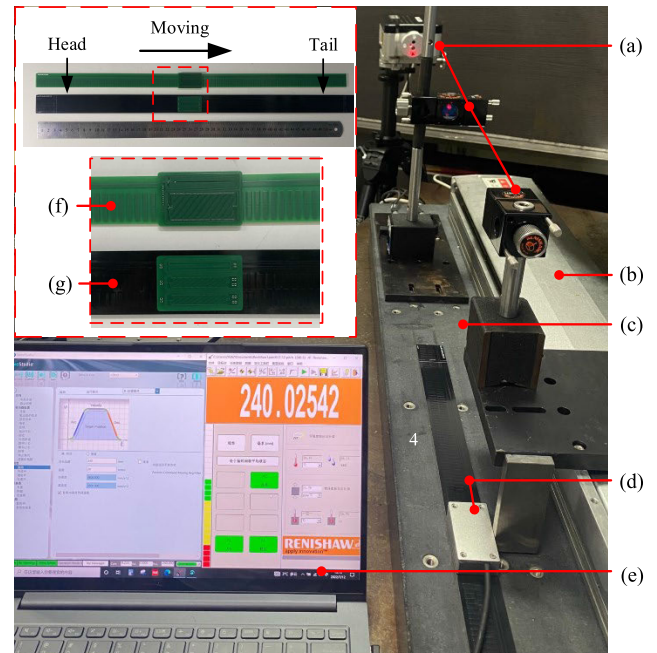

Fig. 4. Sensor prototype and experimental platform. (a) Laser interferometer; (b) linear motor; (c) marble platform; (d) the proposed sensor; (e) DAQ interface; (f) the sensor before optimization; and (g) the sensor after optimization.

demonstrates that the structure and the measurement principle are feasible.

IV. SENSOR PROTOTYPE AND PRIMARY EXPERIMENTS
A. Sensor Prototype and Experimental Platform

In order to evaluate the effectiveness and accuracy of the sensor, a sensor prototype is manufactured by printed circuit board (PCB) technology with a manufacturing accuracy of 10 μm, as shown in Fig. 4. The key parameters of the sensor prototype are adopted as follows: the total length of the stationary component is 516 mm, and the available measurement range is 500 mm, wherein the pitch of the fine measurement channel is 4 mm, while the number of pitches is $N = 150$.
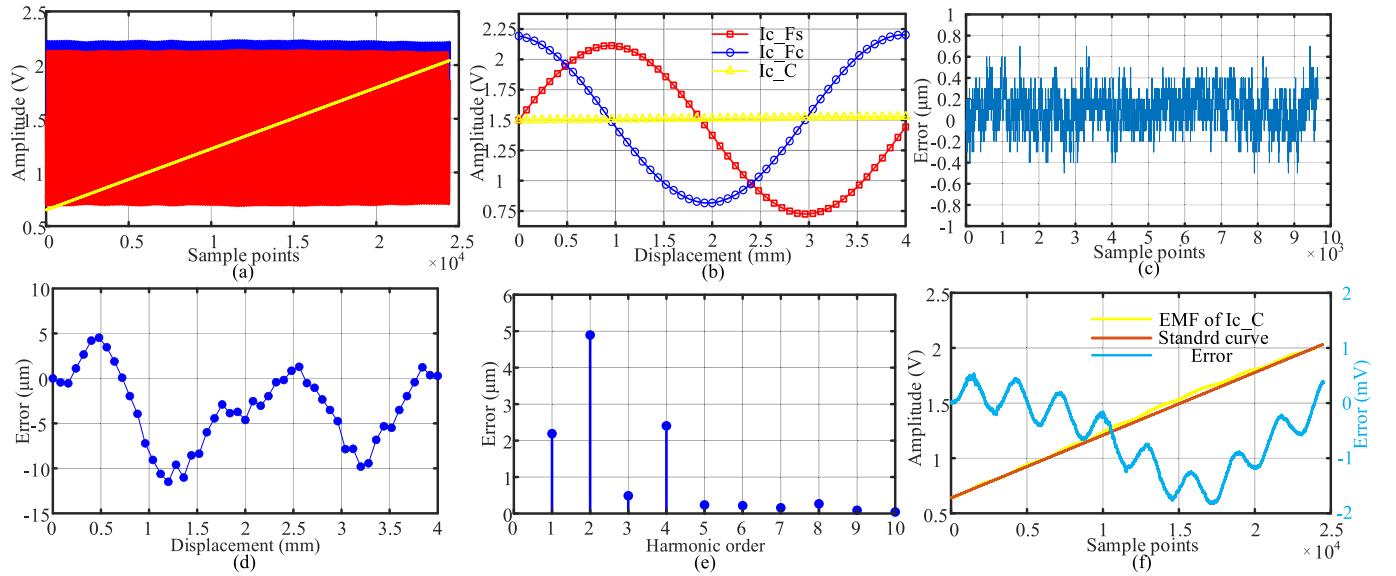
Fig. 5. Primary experimental results. (a) Output signal of inductive coils after demodulation, filtering, and amplification in the full range; (b) the output signal of inductive coils in a pitch; (c) the stability of the sensor for 12 h; (d) the in-pitch error of; (e) the spectral result of (d); and (f) the error analysis of the inductive signal of Ic_C.

TABLE II
PARAMETERS OF THE PCB MANUFACTURE TECHNIQUE

Parameters	Stationary component	Movable component
Layer number	1	2
Track width	NA	0.1 mm
Track clearance	NA	0.1 mm
Copper thickness	0.035 mm	0.035 mm
Through hole diameter	NA	0.2 mm
Machining tolerances	0.01 mm	0.01 mm

The thickness of the mental reflection conductors D_F is larger than the skin depth of the metal reflection conductors

$$D_F > \delta = \sqrt{2/\omega\mu\sigma}. \tag{7}$$

Here, δ is the depth of penetration, ω is the angular frequency of the excitation signal (4 MHz), μ is the magnetic permeability of copper (1.257×10^{-6} H/m), and σ is the conductivity of the metal reflection conductors (5.8×10^7 Ω/m). The parameters μ and σ both are constant; therefore, the parameter D_F is determined by the frequency of the excitation signal. The frequency of the sensor is 4 MHz, and the skin depth of the mental reflection conductors is about 0.166 mm. The remaining parameters and PCB layout of the sensor prototype are shown in Table II.

The experimental platform is shown in Fig. 4. The stationary component of the sensor prototype is mounted onto the marble platform with a machining accuracy of 10 μm. The movable component of the sensor prototype and the signal processing circuit both are placed in an aluminum box, which is mounted onto the sliding table of the linear motor. The parallelism of the sensor prototype and the linear motor is kept below 10 μm. A Renishaw XL80 laser interferometer with ±0.5 ppm precision served as the measurement standard to calibrate the sensor prototype.

B. Primary Experiments

The sensor prototype is used as the position feedback to drive the motor at the speed of 5 mm/s. The output signals of inductive coils after demodulation, filtering, and amplification in the full range are shown in Fig. 5(a). The red line and the blue line are sine signals and cosine signals of Ic_Fs and Ic_Fc respectively, which change periodically within the full range. The yellow line is the output signal of Ic_C, which changes linearly within the range and can realize coarse positioning. For clarity, only the signal in one measurement period is shown in Fig. 5(b).

The sensor shows good stability, as shown in Fig. 5(c). Keep the sensor still and sample every 5 s for more than 12 h, and the peak-to-peak stability fluctuation is 1.1 μm. The in-pitch error over the pitch of 4 at 0.08 mm intervals, is shown in Fig. 5(d). The spectral analysis result obtained by fast Fourier transform (FFT) is shown in Fig. 5(e). The experiment results show that the in-pitch error is about 9.3 μm, and it mainly involves the first-, second-, and fourth-order harmonic components. The linearity of Ic_C's inductive signal determines the absolute positioning ability of the sensor, and the experiment analysis results are shown in Fig. 5(f), with the maximum error being about 1.8 mV. Further analysis of the causes of the in-pitch errors and methods to suppress them will be analyzed in the next section.

V. IMPROVED DESIGNS AND FINAL EXPERIMENTS
A. Error Analysis

1) First Order Error: The first-order error is mainly caused by the invalid EMF. Ideally, the output signals of Ic_F should be zero when the stationary component is not working. However, the magnetic flux in the inductive coils cannot be

completely offset because of the difficulty in achieving an ideal state in the manufacturing, installation, and leading wire of the movable component, which results in an invalid EMF. When the movable component and the stationary component have relative displacement, the output signals of the inductive coils contain components that are not related to the displacement because of the invalid EMF. The inductive EMFs at this time can be shown as follows:

$$e_{\text{Ic\_Fs}}(t, x) = k_1 \sin(\omega t) \sin\left(\frac{2\pi}{W}x_2\right) + k_{11} \sin(\omega t) \qquad (8)$$

$$e_{\text{Ic\_Fc}}(t, x) = k_1 \sin(\omega t) \cos\left(\frac{2\pi}{W}x_2\right) + k_{12} \sin(\omega t). \qquad (9)$$

Here, k_{11} and k_{12} are the dc component of the inductive EMFs of Ic_Fs and Ic_Fc respectively. According to (3), (8), and (9), the displacement including the theoretical error Δx can be expressed as follows:

$$x_{2\_1} = \frac{W}{2\pi} \arctan\left(\frac{k_1 \sin(\omega t) \sin\left(\frac{2\pi}{W}x_2\right) + k_{11} \sin(\omega t)}{k_1 \sin(\omega t) \cos\left(\frac{2\pi}{W}x_2\right) + k_{12} \sin(\omega t)}\right). \qquad (10)$$

Therefore, the theoretical error Δx can be expressed as follows:

$$\Delta x = x_{2\_1} - x_2 = \frac{W}{2\pi} \arctan\left(\frac{\frac{k_1 \sin\left(\frac{2\pi}{W}x\right) + k_{11}}{k_1 \cos\left(\frac{2\pi}{W}x\right) + k_{12}} - \frac{\sin\left(\frac{2\pi}{W}x\right)}{\cos\left(\frac{2\pi}{W}x\right)}}{1 + \frac{k_1 \sin\left(\frac{2\pi}{W}x\right) + k_{11}}{k_1 \cos\left(\frac{2\pi}{W}x\right) + k_{12}} \frac{\sin\left(\frac{2\pi}{W}x\right)}{\cos\left(\frac{2\pi}{W}x\right)}}\right)$$

$$= \frac{W}{2\pi} \sqrt{k_{11}^2 + k_{12}^2} \sin\left(\frac{2\pi}{W}x + \arctan\left(\frac{k_{11}}{k_{12}}\right)\right). \qquad (11)$$

The theoretical error Δx changes for a period within a pitch. Therefore, the first-order error will be introduced when the manufacturing, installation, and leading wire of the sensor are not ideal.

2) Second Order Error: According to the measurement principle, the amplitude of the two roads of inductive EMFs should be equal, and the phase should be orthogonal. However, the manufacturing, installation, leading wire, and signal processing of the sensor may lead to the problem of unequal amplitude or non-orthogonal phase, which will lead to measurement errors.

When the amplitudes of te unequal, the signals can be shown as follows:

$$e_{\text{Ic\_Fs}}(t, x) = k_{21} \sin(\omega t) \sin\left(\frac{2\pi}{W}x\right) \qquad (12)$$

$$e_{\text{Ic\_Fc}}(t, x) = k_{22} \sin(\omega t) \cos\left(\frac{2\pi}{W}x\right). \qquad (13)$$

Here, k_{21} and k_{22} are the amplitude of the two roads of inductive EMFs, and $k_{21} \neq k_{22}$. According to (3), (12), and (13), the displacement including the theoretical error Δx can be expressed as follows:

$$x_{2\_2} = \frac{W}{2\pi} \arctan\left(\frac{k_{21} \sin\left(\frac{2\pi}{W}x_2\right)}{k_{22} \cos\left(\frac{2\pi}{W}x_2\right)}\right). \qquad (14)$$

The theoretical error Δx can be expressed as follows:

$$\Delta x = x_{2\_3} - x_2 = \frac{W}{2\pi} \arctan\left(\frac{\frac{k_{11} \sin\left(\frac{2\pi}{W}x + \Delta\varphi\right)}{k_{12} \cos\left(\frac{2\pi}{W}x\right)} - \frac{\sin\left(\frac{2\pi}{W}x\right)}{\cos\left(\frac{2\pi}{W}x\right)}}{1 + \frac{k_{11} \sin\left(\frac{2\pi}{W}x + \Delta\varphi\right)}{k_{12} \cos\left(\frac{2\pi}{W}x\right)} \frac{\sin\left(\frac{2\pi}{W}x\right)}{\cos\left(\frac{2\pi}{W}x\right)}}\right)$$

$$= \frac{W}{2\pi} \frac{k_{21} - k_{22}}{k_{22}} \sin\left(2\frac{2\pi}{W}x\right). \qquad (15)$$

When the phases of the inductive EMFs are non-orthogonal, the signals can be shown as follows:

$$e_{\text{Ic\_Fs}}(t, x) = k \sin(\omega t) \sin\left(\frac{2\pi}{W}x + \Delta\varphi\right) \qquad (16)$$

$$e_{\text{Ic\_Fc}}(t, x) = k \sin(\omega t) \cos\left(\frac{2\pi}{W}x\right). \qquad (17)$$

Here, $\Delta\varphi$ is the phase difference between the two roads of signals. According to (3), (16), and (17), the displacement including the theoretical error Δx can be expressed as follows:

$$x_{2\_3} = \frac{W}{2\pi} \arctan\left(\frac{\sin\left(\frac{2\pi}{W}x_2 + \Delta\varphi\right)}{\cos\left(\frac{2\pi}{W}x_2\right)}\right). \qquad (18)$$

The theoretical error Δx can be expressed as follows:

$$\Delta x = x_{2\_3} - x_2 = \frac{W}{2\pi} \arctan\left(\frac{\frac{k_{11} \sin\left(\frac{2\pi}{W}x + \Delta\varphi\right)}{k_{12} \cos\left(\frac{2\pi}{W}x\right)} - \frac{\sin\left(\frac{2\pi}{W}x\right)}{\cos\left(\frac{2\pi}{W}x\right)}}{1 + \frac{k_{11} \sin\left(\frac{2\pi}{W}x + \Delta\varphi\right)}{k_{12} \cos\left(\frac{2\pi}{W}x\right)} \frac{\sin\left(\frac{2\pi}{W}x\right)}{\cos\left(\frac{2\pi}{W}x\right)}}\right)$$

$$= \frac{W}{2\pi} \sin\left(\frac{\Delta\varphi}{2}\right) \cos\left(2\frac{2\pi}{W}x + \frac{\Delta\varphi}{2}\right) + \frac{W}{4\pi} \sin(\Delta\varphi). \qquad (19)$$

Unequal amplitude and non-orthogonal phase will cause the theoretical error Δx to change for two periods within a pitch. Therefore, the second-order error will be introduced.

3) Fourth Order Error: The two roads of inductive EMFs can be expressed by the Fourier series. With the increase of harmonic frequency, the corresponding amplitude decays rapidly. The signals can be expressed as (20) and (21) when only the fundamental and the third-order components are considered

$$e_{\text{Ic\_Fs}}(t, x) = k \sin(\omega t) \left[a_1 \sin\left(\frac{2\pi}{W}x + \varphi_1\right) - a_3 \sin\left(3\frac{2\pi}{W}x + \varphi_3\right)\right] \qquad (20)$$

$$e_{\text{Ic\_Fc}}(t, x) = k \sin(\omega t) \left[a_1 \cos\left(\frac{2\pi}{W}x + \varphi_1\right) + a_3 \cos\left(3\frac{2\pi}{W}x\right) + \varphi_3\right]. \qquad (21)$$

Here, a_1 and a_3 are the amplitude of the fundamental and the third order components, and the φ_1 and φ_3 is the phase respectively. According to (3), (18), and (19), the displacement including the theoretical error Δx can be expressed as follows:

$$x_{2\_3} = \frac{W}{2\pi} \arctan \left(\frac{a_1 \sin\left(\frac{2\pi}{W}x\right) - a_3 \sin\left(3\frac{2\pi}{W}x + \varphi_3\right)}{a_1 \cos\left(\frac{2\pi}{W}x\right) + a_3 \cos\left(3\frac{2\pi}{W}x\right) + \varphi_3} \right). \tag{22}$$

The theoretical error Δx can be expressed as follows:

$$\Delta x = x_{2\_2} - x_2$$

$$= \frac{W}{2\pi} \arctan \left(\frac{\frac{a_1 \sin\left(\frac{\pi}{W}x + \varphi_1\right) - a_3 \sin\left(\frac{2\pi}{W}x + \varphi_3\right)}{a_1 \cos\left(\frac{2\pi}{W}x + \varphi_1\right) + a_3 \cos\left(\frac{2\pi}{W}x + \varphi_3\right)} - \frac{\sin\left(\frac{2\pi}{W}x\right)}{\cos\left(\frac{2\pi}{W}x\right)}}{1 + \frac{a_1 \sin\left(\frac{2\pi}{W}x + \varphi_1\right) - a_3 \sin\left(\frac{2\pi}{W}x + \varphi_3\right)}{a_1 \cos\left(\frac{2\pi}{W}x + \varphi_1\right) + a_3 \cos\left(\frac{2\pi}{W}x + \varphi_3\right) \sin\left(\frac{2\pi}{W}x\right)}} \right)$$

$$= \frac{W}{2\pi} a_3 \tan(\varphi_1) \sin\left(4\frac{2\pi}{W}x + \varphi_3\right). \tag{23}$$

The theoretical error Δx changes for four periods within a pitch. Therefore, the fourth-order error is introduced as a systematic error.

B. Improved Designs

According to the analysis in the previous section, the first-order error in a pitch is mainly caused by the invalid EMF, which can be suppressed by the dc component in compensation (12) and (11). The specific methods that can be used in the experiment are as follows. First, when the stationary component is not involved in the work, obtain and memorize the value after analog-to-digital conversion, that is, the value of invalid EMF (k_{11} and k_{12}). Then, when the sensor prototype works normally, the two inductive EMFs are subtracted from the memorized k_{11} and k_{12} respectively. And the arctangent operation is carried out, so as to reduce or eliminate the influence of invalid EMF.

For the second-order error, the compensation method is also used to suppress it. The specific methods that can be used in the experiment are as follows. First, move the movable component for numbers of pitches, obtain and memorize the average amplitude (k_{21} and k_{22}) of the two roads of inductive EMFs after analog-to-digital conversion, and calculate the ratio of larger amplitude to smaller amplitude. Take this ratio as the second error compensation coefficient. When the sensor prototype works normally, multiply the small-amplitude signal by the compensation coefficient during the calculation to suppress the second-order error.

The fourth-order error is caused by the third harmonic component, which can be suppressed by eliminating the harmonic component. The third harmonic component is often eliminated by spatial phase shifting. The precise measurement channel is divided into two parts and staggered $W/6$ to form a differential structure. The optimized sensor is shown in Fig. 6.
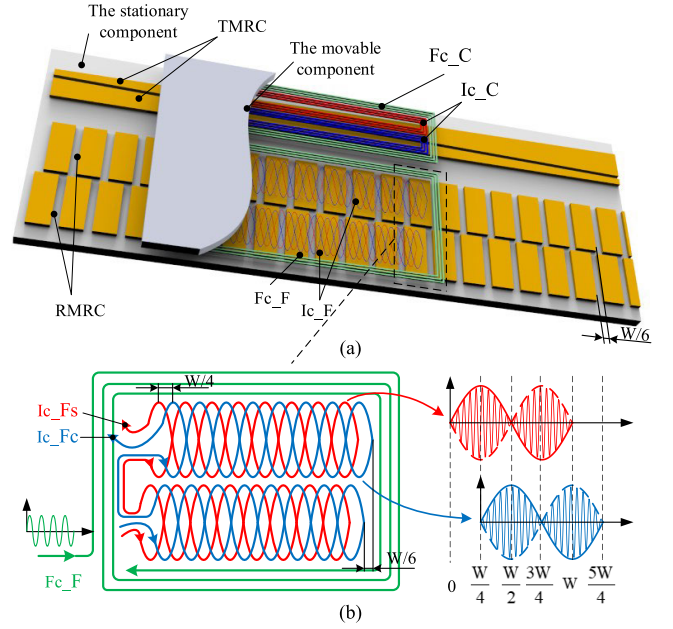

Fig. 6. Structure diagram of the optimized sensor.

The inductive EMFs can be expressed as follows:

$$e'_{\text{Ic\_Fs}}(t, x) = A \sin(\omega t) \left[a_1 \sin\left(\frac{2\pi}{W}x + \varphi_1\right) \right.$$
$$\left. - a_3 \sin\left(3\frac{2\pi}{W}x + \varphi_3\right) \right] \tag{24}$$

$$e''_{\text{Ic\_Fs}}(t, x) = A \sin(\omega t) \left[a_1 \sin\left(\frac{2\pi}{W}\left(x + \frac{W}{6}\right) + \varphi_1\right) \right.$$
$$\left. - a_3 \sin\left(3\frac{2\pi}{W}\left(x + \frac{W}{6}\right) + \varphi_3\right) \right] \tag{25}$$

where $e_{\text{Ic\_Fs}}(t, x)$ is the sum of $e'_{\text{Ic\_Fs}}(t, x)$ and $ee''_{\text{Ic\_Fs}}(t, x)$ superposed as follows.

$$e_{\text{Ic\_Fs}}(t, x) = e'_{\text{Ic\_Fs}}(t, x) + e''_{\text{Ic\_Fs}}(t, x)$$
$$= 2\sqrt{3} A a_1 \sin(\omega t) \sin\left(\frac{2\pi}{W}x + \varphi_1 - \frac{\pi}{6}\right). \tag{26}$$

It can be known from (26) that the third harmonic component is eliminated. Therefore, the fourth-order error can be suppressed.

At the same time, aiming at the disadvantage that the amplitude variation of the coarse measurement channel is not obvious, the differential structure is used for optimization, as shown in Fig. 6. The sensitivity of the optimized structure is improved, and it has the advantages of eliminating the zero value and canceling the common-mode interference.

C. Final Experiments

The same method is used to test the effectiveness and accuracy of the optimized sensor model. The in-pitch error and spectral analysis results before and after optimization are shown in Fig. 7. It can be shown that the first- and second-order errors have decreased significantly. Assume that the center position of the left side of the stationary component
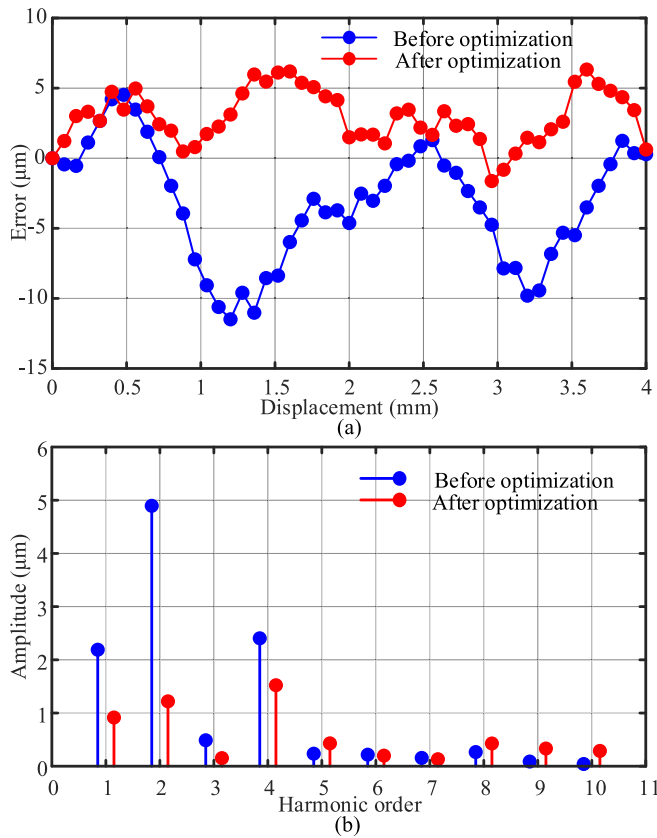
Fig. 7. Measurement results in a pitch. (a) Measurement errors before and after optimization. (b) Spectral analysis result of (a).
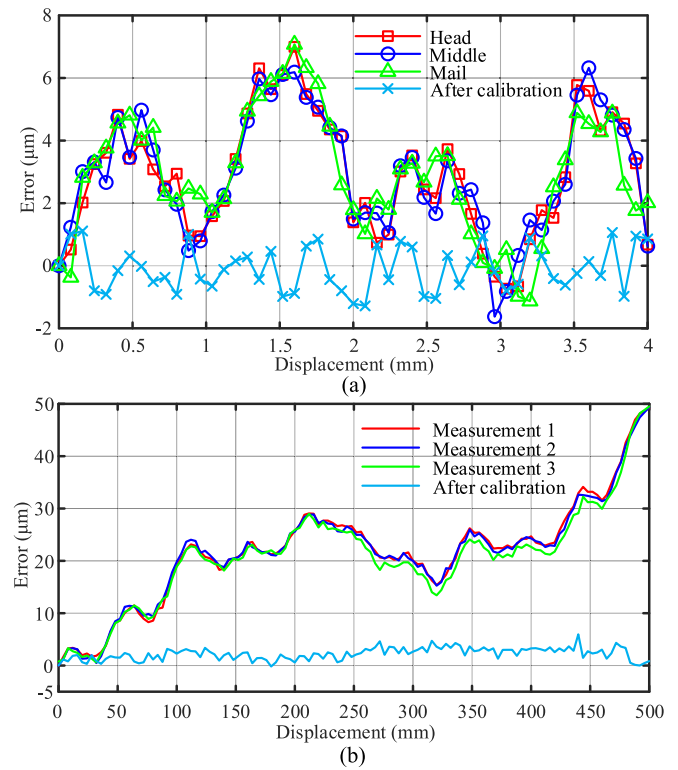

Fig. 8. Final measurement results. (a) Measurement errors in a pitch. (b) Measurement errors in the full range.

Fig. 9. Measurement channel interference experiment. (a) Coarse measurement channel interference experiment. (b) Coarse fine channel interference experiment.

coincides with the movable component is the zero point. Three pitches respectively located in the head, middle, and tail of the stationary component, which are 20, 250, and 480 mm away from the zero point, as shown in Fig. 4, are selected to carry out a static measurement experiment with a step length of 0.08 mm. The in-pitch measurement errors are shown in Fig. 8(a). The worst-case errors are 6.99, 6.52, 7.07, and 6.75 μm, respectively. The sensor shows good repeatability at different pitches, and the worst-case error after correction by the point-by-point compensation method is -1.29 μm, therefore, the linearity for a pitch is 0.03%.

The full-range worst-case error with a step length of 4 mm over 500 mm is tested, and the full-range error curve is shown in Fig. 8(b). The full-range error increases with displacement, and the worst-case error at different measurement times are 49.2, 49.35, and 49.51 μm, respectively. The error is mainly accumulated by the deviation in the metal reflection conductors at each pitch, which is a systematic manufacturing error. In addition, the deviation of installation over the full range is also the main cause of the error. The full-range worst-case error after calibrating is -3.81 μm.

In order to verify whether the two measurement channels interfere with each other, the two channels are tested alone. The results of the experiment, as shown in Fig. 9, indicate that the two measurement channels do have some interference. However, the maximum voltage error value of the coarse measurement channel is -1.8 mV, which is far lower than the range of voltage variation within the pitch, and does not affect

its polar positioning ability. When the precision measurement channel is working alone, the worst-case error is 3.51 μm, which is slightly lower than when two measurements are

TABLE III
COMPREHENSIVE COMPARISON OF THE MAJOR TYPES OF DISPLACEMENT SENSORS USED FOR PRECISION POSITIONING. THE FIGURES QUOTED ARE REPRESENTATIVE OF COMMERCIALLY AVAILABLE DEVICES AND DO NOT INDICATE ANY THEORETICAL LIMITS

Sensor type	Range (mm)	Resolution/ Linearity	Cost	Easy to Manufacture	sensitivity	compactness	stability	Tolerance to environment
Laser interferometers[13]	Up to 80000	Excellence	Expensive	Limited	Excellence	Limited	Pass	Fragile
Optical linear encoders[18]	Up to 3040	Excellence	Expensive	Limited	Excellence	Excellence	Excellence	Fragile
Capacitive sensors[26]	200	Excellence	Pass	Pass	Excellence	Excellence	Pass	Fragile
Inductive sensors[30]	300	Pass	Pass	Excellence	Pass	Excellence	Pass	Excellence
Eddy current sensors[38]	10^{-2}	Excellence	Pass	Excellence	Excellence	Excellence	Pass	Excellence
This paper	500	Moderate	Pass	Excellence	Moderate	Excellence	Pass	Excellence

used simultaneously. Finally, the sensor proposed in this article is compared with some typical linear displacement sensors, as shown in Table III.

VI. CONCLUSION

This article proposed a high-precision and large-range absolute linear displacement sensor based on the eddy current effect. First of all, the sensor structure and measurement principle are proposed. Then, a 3-D model of the sensor is established and the electromagnetic field simulation is carried out to verify the feasibility of the sensor. The sensor prototype is fabricated by PCB technology and the experimental platform is built up for testing the performance of the sensor prototype. Finally, error analysis and structure optimization are proposed. According to the theoretical analysis and experimental verification, the conclusions are summarized as follows:

1) The sensor is composed of a coarse measurement channel and a fine measurement channel. The coarse measurement channel is used to realize pitch positioning and determine the approximate position of the sensor. The fine measurement channel obtains high-precision linear displacement measurements composed of N measurement periods. Combining the measurements of the coarse measurement channel and the fine measurement channel yields high-precision absolute linear position measurements. Compared with the absolute positioning of multiple pairs of measurement periods, the absolute position coding of the sensor is simpler.

2) The first-order error of the sensor is mainly caused by invalid EMF, and the second-order error is mainly caused by the unequal amplitude and non-orthogonal phase of the two roads of inductive EMFs, which can be suppressed by the means of signal compensation. The fourth-order error is mainly caused by the third harmonic component of the inductive EMFs, which can be suppressed by spatial phase shifting.

3) The resolution of the sensor is 0.25 μm, and the linearity for a pitch is 0.03%, while it is 0.0762% for the full measurement range.

In addition, the sensor has the characteristics of a simple structure, low cost, easy manufacture, and strong anti-interference ability, which demonstrated excellent prospects for further commercialization and applications. In the following work, we will focus on further structure optimization, error analysis, and error correction technology to improve the performance of the sensor.

REFERENCES

[1] N. Anandan and B. George, "A wide-range capacitive sensor for linear and angular displacement measurement," *IEEE Trans. Ind. Electron.*, vol. 64, no. 7, pp. 5728–5737, Jul. 2017.

[2] A. J. Fleming, "A review of nanometer resolution position sensors: Operation and performance," *Sens. Actuators A, Phys.*, vol. 190, pp. 106–126, Feb. 2013.

[3] K. Peng, Z. Yu, X. Liu, Z. Chen, and H. Pu, "Features of capacitive displacement sensing that provide high-accuracy measurements with reduced manufacturing precision," *IEEE Trans. Ind. Electron.*, vol. 64, no. 9, pp. 7377–7386, Sep. 2017.

[4] Y. K. Kim, K. S. Kim, and S. Kim, "A portable and remote 6-DOF pose sensor system with a long measurement range based on 1-D laser sensors," *IEEE Trans. Ind. Electron.*, vol. 62, no. 9, pp. 5722–5729, Sep. 2015.

[5] X. K. Liu et al., "High-precision multi-turn absolute time-grating angular displacement sensor based on re-modulation scheme," *Chin. J. Sci. Instrum.*, vol. 42, no. 5, pp. 90–98, May 2021.

[6] L. Wu et al., "An absolute linear displacement sensor based on orthogonal dual traveling wave magnetic field," *IEEE Sensors J.*, vol. 22, no. 6, pp. 6019–6026, Feb. 2022.

[7] W. Gao et al., "Measurement technologies for precision positioning," *CIRP Ann.*, vol. 64, no. 2, pp. 773–796, Jan. 2015.

[8] X. Li et al., "Two-probe optical encoder for absolute positioning of precision stages by using an improved scale grating," *Opt. Exp.*, vol. 24, no. 19, pp. 21378–21391, Sep. 2016.

[9] B. George, Z. Tan, and S. Nihtianov, "Advances in capacitive, eddy current, and magnetic displacement sensors and corresponding interfaces," *IEEE Trans. Ind. Electron.*, vol. 64, no. 12, pp. 9595–9607, Dec. 2017.

[10] B. Sun and B. Li, "A quantitative error compensation model of the inclination angle of the laser displacement sensor," *Chin. J. Sci. Instrum.*, vol. 36, no. 5, pp. 996–1004, 2015.

[11] M. Fu, C. Li, G. Zhu, H. Shi, and F. Chen, "A high precision time grating displacement sensor based on temporal and spatial modulation of light-field," *Sensors*, vol. 20, no. 3, p. 921, Feb. 2020.

[12] P. Schellekens et al., "Design for precision: Current status and trends," *CIRP Ann.*, vol. 47, no. 2, pp. 557–586, Feb. 1998.

[13] (Feb. 4, 2023). *RENISHAW Apply Innovation*. [Online]. Available: https://www.renishaw.com.cn

[14] R. K. Heilmann, C. G. Chen, P. T. Konkola, and M. L. Schattenburg, "Dimensional metrology for nanometre-scale science and engineering: Towards sub-nanometre accurate encoders," *Nanotechnology*, vol. 15, no. 10, pp. 504–511, Jul. 2004.

[15] X. Liu, K. Peng, Z. Chen, H. Pu, and Z. Yu, "A new capacitive displacement sensor with nanometer accuracy and long range," *IEEE Sensors J.*, vol. 16, no. 8, pp. 2306–2316, Apr. 2016.

[16] M. L. Jiang, F. P. Li, and X. D. Wang, "Nano-displacement measurement with grating interference," *Appl. Mech. Mater.*, vol. 103, pp. 35–40, Sep. 2011.

[17] L. Santamaria, C. E. Garcia-Ortiz, H. R. Siller, R. Cortes, and V. Coello, "Optical method for distance and displacement measurements of the probe-sample separation in a scanning near-field optical microscope," *AIP Adv.*, vol. 6, no. 4, Apr. 2016, Art. no. 045007.

[18] *Linear Grating Ruler: Continuous and Steady Measurement and Detailed Precision Data*.

[19] G. Ye et al., "Design and development of an optical encoder with sub-micron accuracy using a multiple-tracks analyser grating," *Rev. Sci. Instrum.*, vol. 88, no. 1, 2017, Art. no. 015003.

[20] G. Ye et al., "Ratiometric-linearization-based high-precision electronic interpolator for sinusoidal optical encoders," *IEEE Trans. Ind. Electron.*, vol. 65, no. 10, pp. 8224–8231, Oct. 2018.

[21] W. Li, N. Cai, Z. Ning, Y. Dong, and H. Wang, "Error compensation for optical encoder via local-sinusoidal-assisted empirical mode decomposition with an optimization scheme," *IEEE Trans. Ind. Electron.*, vol. 69, no. 9, pp. 9596–9604, Sep. 2022.

[22] Y. Ye, C. Zhang, C. He, X. Wang, J. Huang, and J. Deng, "A review on applications of capacitive displacement sensing for capacitive proximity sensor," *IEEE Access*, vol. 8, pp. 45325–45342, 2020.

[23] D. Zhang et al., "Absolute capacitive grating displacement measuring system with both high-precision and long-range," *Sens. Actuators A, Phys.*, vol. 295, pp. 11–22, May 2019.

[24] Z. Yu K. Peng, X. Liu, Z. Chen, and Y. Huang, "A high-precision absolute angular-displacement capacitive sensor using three-stage time-grating in conjunction with a remodulation scheme," *IEEE Trans. Ind. Electron.*, vol. 66, no. 9, pp. 7376–7385, Sep. 2019.

[25] A. S. A. Kumar, N. Anandan, B. George, and S. C. Mukhopadhyay, "Improved capacitive sensor for combined angular and linear displacement sensing," *IEEE Sensors. J.*, vol. 19, no. 22, pp. 10253–10261, Nov. 2019.

[26] X. Liu, R. Huang, Z. Yu, K. Peng, and H. Pu, "A high-accuracy capacitive absolute time-grating linear displacement sensor based on a multi-stage composite method," *IEEE Sensors J.*, vol. 21, no. 7, pp. 8969–8978, Apr. 2021.

[27] W. Fan, M. Chen, H. Jin, and Y. Wang, "Multi-layer concentric ring differential capacitance displacement sensor," *Measurement*, vol. 136, pp. 615–621, Mar. 2019.

[28] L. Wu, Q. Tang, X. Chen, S. Xu, L. Gou, and Y. Wang, "A novel two-dimensional sensor with inductive spiral coils," *IEEE Sensors J.*, vol. 19, no. 13, pp. 4857–4865, Jul. 2019.

[29] K. R. Sandra, A. A. Kumar, B. George, and V. J. Kumar, "A linear differential inductive displacement sensor with dual planar coils," *IEEE Sensors J.*, vol. 19, no. 2, pp. 457–464, Jan. 2019.

[30] J. Zhao, M. Li, S. Peng, Y. Guo, and Q. Tang, "An inductive linear displacement sensor with complementary resonant coupling units," *IEEE Sensors J.*, vol. 21, no. 22, pp. 25659–25667, Nov. 2021.

[31] X. Gu, Q. Tang, D. Peng, and D. Weng, "An inductive linear displacement sensor with bilateral sensing units," *IEEE Sensors J.*, vol. 21, no. 1, pp. 296–305, Jan. 2021.

[32] X. Lu et al., "Research on the time drift stability of differential inductive displacement sensors with frequency output," *Sensors*, vol. 22, no. 16, p. 6234, Aug. 2022.

[33] A. Babu and B. George, "A wide range planar coil based displacement sensor with high sensitivity," in *Proc. IEEE Int. Instrum. Meas. Technol. Conf.*, May 2017, pp. 1–6.

[34] Q. Tang, L. Wu, X. Chen, and D. Peng, "An inductive linear displacement sensor based on planar coils," *IEEE Sensors J.*, vol. 18, no. 13, pp. 5256–5264, Jul. 2018.

[35] R. Romary, S. Jelassi, and J. F. Brudny, "Stator-interlaminar-fault detection using an external-flux-density sensor," *IEEE Trans. Ind. Electron.*, vol. 57, no. 1, pp. 237–243, Jan. 2010.

[36] M. R. Nabavi and S. Nihtianov, "Eddy-current sensor interface for advanced industrial applications," *IEEE Trans. Ind. Electron.*, vol. 58, no. 9, pp. 4414–4423, Sep. 2011.

[37] K. J. W. Pluk, T. A. van Beek, J. W. Jansen, and E. A. Lomonova, "Modeling and measurements on a finite rectangular conducting plate in an eddy current damper," *IEEE Trans. Ind. Electron.*, vol. 61, no. 8, pp. 4061–4072, Aug. 2014.

[38] V. Chaturvedi, J. G. Vogel, K. A. A. Makinwa, and S. Nihtianov, "A 19.8-mW eddy-current displacement sensor interface with sub-nanometer resolution," *IEEE J. Solid-State Circuits*, vol. 53, no. 8, pp. 2273–2283, Aug. 2018.

Peng Tong received the B.S. degree from the Chongqing University of Technology (CQUT), Chongqing, China, in 2020, where he is currently pursuing the M.S. degree in mechanical engineering.

He mainly focuses on intelligent instruments and sensors.

Liang Wu (Member, IEEE) received the M.Eng. degree in measurement technology and instrument from CQUT, Chongqing, China, in 2011, and the Ph.D.Eng. degree in mechanical and electronic engineering from Chongqing University, Chongqing, in 2017.

He is currently an Assistant Researcher with the Engineering Research Center of Mechanical Testing Technology and Equipment, Ministry of Education, CQUT. He mainly focuses on precision measurement technology of displacement and instruments.

Yanchen A received the B.S. degree from the Chongqing University of Technology, Chongqing, China, in 2021, where she is currently pursuing the M.S. degree in mechanical engineering.

She mainly focuses on high-precision displacement measurement technology and sensor research.

Rui Su received the B.S. degree in measurement and control technology and instrument from the Sichuan University of Science and Engineering, Sichuan, China, in 2021. She is currently pursuing the M.S. degree in mechanical engineering with CQUT, Chongqing, China.

She mainly focuses on high-precision displacement measurement technology and sensor research.

Yulong Wu received the B.S. degree from the Institute of Disaster Prevention, Langfang, Hebei, China, in 2021. He is currently pursuing the M.S. degree in instrument science and engineering with CQUT, Chongqing, China.

He mainly focuses on intelligent instruments and sensors.